PCCP

PAPER

View Article Online
View Journal | View Issue

Cite this: *Phys. Chem. Chem. Phys.*, 2015, **17**, 2216

Bimodal crystallization at polymer–fullerene interfaces†

Dyfrig Môn,[a] Anthony M. Higgins,*[a] David James,[a] Mark Hampton,[b] J. Emyr Macdonald,[b] Michael B. Ward,[c] Philipp Gutfreund,[d] Samuele Lilliu[e] and Jonathan Rawle[f]

Received 22nd September 2014,
Accepted 26th November 2014

DOI: 10.1039/c4cp04253k

www.rsc.org/pccp

The growth-kinetics of [6,6]-phenyl C61-butyric acid methyl ester (PCBM) crystals, on two different length-scales, is shown to be controlled by the thickness of the polymer layer within a PCBM–polymer bilayer. Using a model amorphous polymer we present evidence, from *in situ* optical microscopy and grazing-incidence X-ray diffraction (GIXD), that an increased growth-rate of nanoscale crystals impedes the growth of micron-sized, needle-like PCBM crystals. A combination of neutron reflectivity and GIXD measurements, also allows us to observe the establishment of a liquid–liquid equilibrium composition-profile between the PCBM layer and a polymer-rich layer, before crystallization occurs. While the interfacial composition-profile is independent of polymer-film-thickness, the growth-rate of nanoscale PCBM crystals is significantly larger for thinner polymer films. A similar thickness-dependent behavior is observed for different molecular weights of entangled polymer. We suggest that the behavior may be related to enhanced local-polymer-chain-mobility in nanocomposite thin-films.

Introduction

Polymer nanocomposites show promise in a wide range of applications, including charge storage/conduction,[1] membrane-separations[2] and advanced-coatings.[3] In many of these and other uses, control of structure and composition near interfaces or in thin-films is key. One of the most widely investigated applications is in polymer–fullerene solar cells, where control of fullerene (PCBM) aggregation, crystallization and mixing is of crucial importance for device optimization.[4–6] Several previous studies of fullerene and fullerene–polymer films have observed different types of PCBM crystals, including nanoscale crystals[7–9] and larger (micron-sized) crystals.[7,10–13] It has been found that blending of the PCBM with a polymer that has a lower glass-transition-temperature (T_g) than the fullerene can significantly enhance the growth of both PCBM nanocrystals[14] and micron-sized PCBM crystals[15,16] as a consequence of the increased PCBM molecular-mobility.[17] However, what is not clear in these blends, is (i) the degree to which the growth of these two forms of PCBM crystal impact on one another, and (ii) the influence of the polymer on these potentially competitive crystal-growth mechanisms. In this paper we provide significant insight into both of these issues using model fullerene–polymer bilayers. The simplified film morphology of bilayers (*cf.* blends) enables excellent characterization of local composition and structure, allowing us to clearly establish the impact of the polymer layer on both nanocrystal and micron-sized crystal growth.

The effects of aggregation, crystallization and mixing on the performance of fullerene–polymer blend devices are complex. PCBM aggregation and crystallization impact charge separation and transport,[5,9,18] with micron-sized crystals reducing the PCBM/polymer-rich-phase interfacial area and hence device efficiency.[13] In some polymer–fullerene mixtures thermal-annealing causes nanoscale coarsening of PCBM aggregates, which improves charge-transport *via* a proposed mechanism of increased PCBM connectivity.[19] In other blends, reduced PCBM content and therefore connectivity within the polymer-rich phase, which accompanies PCBM aggregation, is suggested to explain impeded electron-transport after annealing.[20] Film-thickness is also known to impact the crystal microstructure and charge mobility of conjugated polymers,[21] and the local composition of conjugated-polymer–fullerene blends.[22]

[a] *College of Engineering, Swansea University, Singleton Park, Swansea, SA2 8PP, UK. E-mail: a.m.higgins@swansea.ac.uk*
[b] *School of Physics and Astronomy, Cardiff University, The Parade, Cardiff CF24 3AA, UK*
[c] *Institute for Materials Research, School of Process, Environmental and Materials Engineering, University of Leeds, Leeds, LS2 9JT, UK*
[d] *Institut Laue-Langevin, 71 avenue des Martyrs, 38000 Grenoble, France*
[e] *Nano-Optics and Optoelectronics Research Laboratory, Masdar Institute of Science and Technology, Block 3, Masdar City, PO Box 54224, Abu Dhabi, United Arab Emirates*
[f] *Diamond Light Source, Harwell Science and Innovation Campus, Didcot, Oxfordshire OX11 0DE, UK*

† Electronic supplementary information (ESI) available. See DOI: 10.1039/c4cp04253k

In amorphous polymers, increased local-chain-mobility with reduced film-thickness is reported[23] due to the proximity of free-interfaces.[24] However, apart from two studies,[25,26] the impact of polymer-chain-mobility near interfaces within the nanoscale structures and thin-films used in polymer-based electronic devices has received little attention. In this paper we examine the role of polymer-interface-controlled PCBM-crystallization-kinetics in determining the structure within fullerene–polymer films. This examination is realized by performing a systematic study in which we vary the thickness of the polymer layer within PCBM–polymer bilayers.

The most extensively studied conjugated-polymer–fullerene blend used for solar cells is PCBM–poly(3-hexylthiophene) (P3HT). Recent investigations of mixing and crystallinity in PCBM–P3HT, using bilayers,[27–32] find significant miscibility between PCBM and amorphous P3HT. Here we use bilayers to understand the interplay between fullerene crystallization, polymer–fullerene mixing and polymer-film-thickness. We describe a new phenomenon, in which the polymer-mediated molecular-mobility of PCBM significantly impacts the growth of two forms of PCBM crystals on different length-scales (nanometer-sized crystals and micron-sized needle-like crystals). By investigating the interaction between these two forms of crystal in a bilayer geometry, rather than in a blend, we are able to (i) characterize the composition-profile during crystallization, and (ii) study the role of polymer-film-thickness on PCBM crystal growth. The paper reports some findings for PCBM–P3HT bilayers, but we mostly focus on the well-studied amorphous polymer, atactic polystyrene (PS), of weight-average-molecular-weight (M_w) 344 kg mol^{-1} (344k) and 106 kg mol^{-1} (106k) (both above the entanglement M_w).[33]

Experimental methods

Materials

PCBM with 99.5% purity, was obtained from Solenne. PS, with polydispersity indices of 1.05 and 1.06 for the 344k and 106k batches respectively, was obtained from Polymer Source. P3HT (regioregularity >91%) was supplied by Rieke Metals. Silicon ((100) with native oxide layer) was obtained from Prolog Semicor. Mica sheets were obtained from Goodfellow. Toluene and chlorobenzene were purchased from Sigma-Aldrich.

Sample fabrication

Polymer layers were spin-coated onto freshly-cleaved mica from toluene solutions. PCBM layers were spin-coated from chlorobenzene solutions onto three different substrates; (i) silicon squares ($\sim$1 cm^2) for GIXD, atomic force microscopy (AFM) and optical microscopy; (ii) 2-inch-diameter silicon-blocks for neutron reflectivity (NR); (iii) mica for transmission-electron-microscopy (TEM) and selected-area-electron-diffraction (SAED). Layer thickness was controlled *via* the solution concentration and the spin-speed of the spin-coater. The spin-coated mica/polymer layers and substrate/PCBM layers were then left for 24 hours under vacuum before bilayer fabrication. Silicon–PCBM–polymer bilayers were prepared by floating the polymer layer onto the surface of de-ionized water, and then depositing this layer onto the silicon–PCBM sample (see schematic diagram S21 in ESI†). TEM–SAED samples were prepared in a similar way (the only difference was that these samples were fabricated on mica, rather than silicon, substrates). Newly fabricated bilayers were firstly allowed to dry at ambient conditions and were then left under vacuum for 24 hours, before annealing. After annealing TEM–SAED bilayers were then floated onto the surface of de-ionized water and picked up on grids (Agar) with and without a holey-carbon support film (they were then dried again under ambient conditions and then vacuum). Optical microscopy experiments were performed using two protocols; (i) the silicon was used as-received and (ii) the silicon was used after sonication in acetone and isopropanol for 15 minutes, followed by rinsing with de-ionized water, and drying with nitrogen. The observed growth-curve behavior was not significantly affected by the choice of protocol. The NR samples were prepared using protocol (i) and the GIXD samples using protocol (ii).

Ex situ annealing

Ex situ annealed samples for optical microscopy and NR were annealed in the dark in a vacuum oven (Binder) with a vacuum of $\sim 10^{-3}$ Torr. Sample surface temperatures were calibrated by attaching an external thermocouple to the surface of duplicate silicon samples in the oven. At the end of annealing, samples were removed from the oven and rapidly quenched on a metal surface at room temperature. Bilayer samples for TEM–SAED were annealed using the same procedure, except that the corners of the mica were clamped down to ensure good contact with the oven shelf. Samples for the GIXD measurements were annealed in the dark using a heating stage (Linkam THM3600) within a nitrogen environment and were then rapidly quenched onto a metal surface (the quench was performed within the nitrogen environment). All quoted temperatures for *ex situ* annealed samples refer to the sample surface temperature.

Optical microscopy

Images were obtained using a microscope (Nikon Eclipse-E600FN) with a camera (Hamamatsu Orca-ER) and MetaVue image-acquisition software (Molecular Devices). *In situ* annealing was performed using a Linkam heating-stage containing a nitrogen environment, and a $\times$20 objective. All of the growth-curves presented in the main paper were collected using a tungsten-halogen lamp on the microscope. 'Continuous illumination' consisted of the microscope shutter remaining open during annealing, with images taken at 30 s, 1 minute or 2 minute intervals. 'Intermittent illumination' consisted of around 30 images being taken over an $\sim$4 hour period, with the shutter only being opened for around 2 s when each image was taken. Corroboration that the growth of needle-like crystals was not significantly affected by the illumination was obtained by comparison between the typical lengths of crystals in illuminated and non-illuminated areas of each sample at the end of annealing. Given the potential sensitivity of fullerenes to ultraviolet (UV) and visible light, we also repeated the *in situ* annealing measurements using a mercury

lamp (Osram HBO 103 W/2) on the microscope. Similar PS-thickness-dependent behavior was obtained for the two illumination sources (see ESI† for the mercury lamp data and analysis). Growth-curves were only extracted for needle-like crystals that grew in two opposite directions from a central starting nucleus, and gave a straight final crystal. Model growth-curves were fitted to length-*versus*-time data using the integral fitting code within Origin Pro 9.0 (OriginLab).

AFM

Tapping mode was used on a Dimension-3100 (Veeco) or a CE100, (Park), with OTESPA (Bruker) cantilevers.

GIXD

Measurements were performed at the beam-line I07 at Diamond Light Source. Samples were placed inside a helium-filled chamber, mounted on a 2 + 3 circle diffractometer with a hexapod sample stage. Monochromatic X-rays of energy 10 keV were used. Diffraction patterns were detected with a Pilatus silicon photodiode 2M array detector (Dectris). GIXD maps were taken using a range of incident angles, α, above and below the critical angle, α_c. Acquisition times of 10 s were used at each incident angle during these 'α-scans'. Repeat measurements before and after the α-scans were used to confirm that no signal degradation, due to beam-damage to the sample, occurred during this procedure. These samples were then imaged using optical microscopy.

NR

Measurements were carried out using beam-line D17 at the Institut Laue-Langevin (ILL) in time-of-flight mode. Specular reflectivity was extracted using the program COSMOS within the Large-Array-Manipulation-Program (LAMP) distributed by the ILL. Two incident-angles (0.6° and 2.4°) were used to produce a full reflectivity curve, with resolution ranging from 2.3% at low momentum-transfer (q_z), to 4.9% at high q_z. Measurements during *in situ* annealing used a single angle of 1°. This angle just captured the critical edge for all samples, gave a lower q_z range and a lower resolution (between 4.1% and 8.1%), but a higher neutron flux, allowing much shorter acquisition-times. Samples were exposed to the neutron beam for acquisition-times of 30 minutes at 0.6°, 60 minutes at 2.4° and in 30 s time-slices at 1°. Sample surface temperatures during *in situ* annealing were calibrated by attaching an external thermocouple to the surface of duplicate silicon samples. There is a slight temperature overshoot (of a few °C) at the start of *in situ* annealing, and the quoted temperatures of 140 °C and 170 °C (in Fig. 3 and ESI,† Table S1), represent the approximate maximum sample surface temperatures reached during annealing. The time-temperature history of the samples is shown in the ESI,† Fig. S20.

TEM

Images were obtained using a Field-Emission-Gun-Transmission-Electron Microscope (FEI Tecnai TF20) operated at 200 kV with a CCD Camera (Gatan Orius SC600A). SAED images were captured using a 250 mm camera length with a selected area approximately 180 nm in diameter on the specimen. The camera was calibrated using the (111) reflection from a gold standard. To determine whether the sample was being degraded by the focused and intense electron bombardment during SAED, five diffraction patterns from a crystal were acquired after 0, 1, 2, 5 and 10 minutes of continuous exposure. No change in the SAED pattern was observed in this time series.

Results and discussion

Imaging of needle-like PCBM crystal growth

We began our investigations by imaging fullerene crystals in thermally-annealed PCBM–polymer bilayers on silicon substrates, using optical microscopy and AFM. In all samples described in this paper the polymer layer is on top of the PCBM layer. Fig. 1a and b show the emergence of 'needle-like' PCBM crystals in PCBM–polymer bilayers on a silicon substrate. These needles can grow to a length of many microns, but are absent from regions of the samples without a polymer layer on top of the PCBM. Fig. 1c shows the influence of PCBM and PS film-thickness on crystal shape and length respectively. The three left-hand images in Fig. 1c (inside the red box) show that the aspect-ratio of the crystals can be controlled *via* PCBM-layer-thickness. Needle-like crystals in PCBM–PS bilayers show uniaxial growth for PCBM layers $\leq$20 nm. For 20 nm PCBM, we obtain needle-like crystals that grow to an average size determined by the thickness of the PS layer (see the two right-hand images in Fig. 1c – inside the green box), plus isotropic crystals (dots) that nucleate but do not grow significantly. By careful choice of PCBM-thickness and annealing-temperature (see ESI,† Fig. S1–S3), we are able to produce isolated needle-like crystals for a range of PS-thicknesses. Fig. 1d shows an AFM image of a needle, showing that the crystal protrudes well above the surrounding bilayer. There is a significant depression in the film on either side of the crystal (as seen in blends[34]), but not in front of the tip. The needle width and growing tip shape are similar for crystals of different length on the same sample, as well as for different annealing-times, PS-thicknesses and M_w (ESI,† Fig. S4–S7). Li *et al.* found that needle-like PCBM crystals in blends were single crystals.[35] A similar conclusion is supported here by polarized-optical-microscopy (ESI,† Fig. S8 and S9) and SAED.

We used *in situ* optical-microscopy to measure the growth of individual needle-like crystals during annealing. Fig. 2a–c show crystal-length against annealing-time, for P3HT-bilayers and two different M_w PS-bilayers, in each case showing growth-curves for crystals that have nucleated after similar annealing-times. In all three cases, significant differences in growth-rates are seen as a function of film-thickness, with significantly longer crystals growing for polymer layers of 35 nm or thicker, in comparison to polymer layers thinner than 16 nm. Crystals in PS bilayers with thicknesses between 16 nm and 25 nm show intermediate behavior, with some variability in the growth-curves in the 344k-PS samples (the majority of crystals on these samples grow to final lengths of ~15–25 μm, but some, particularly on the 25 nm bilayer, grow to ~30–40 μm; see Fig. 2b).

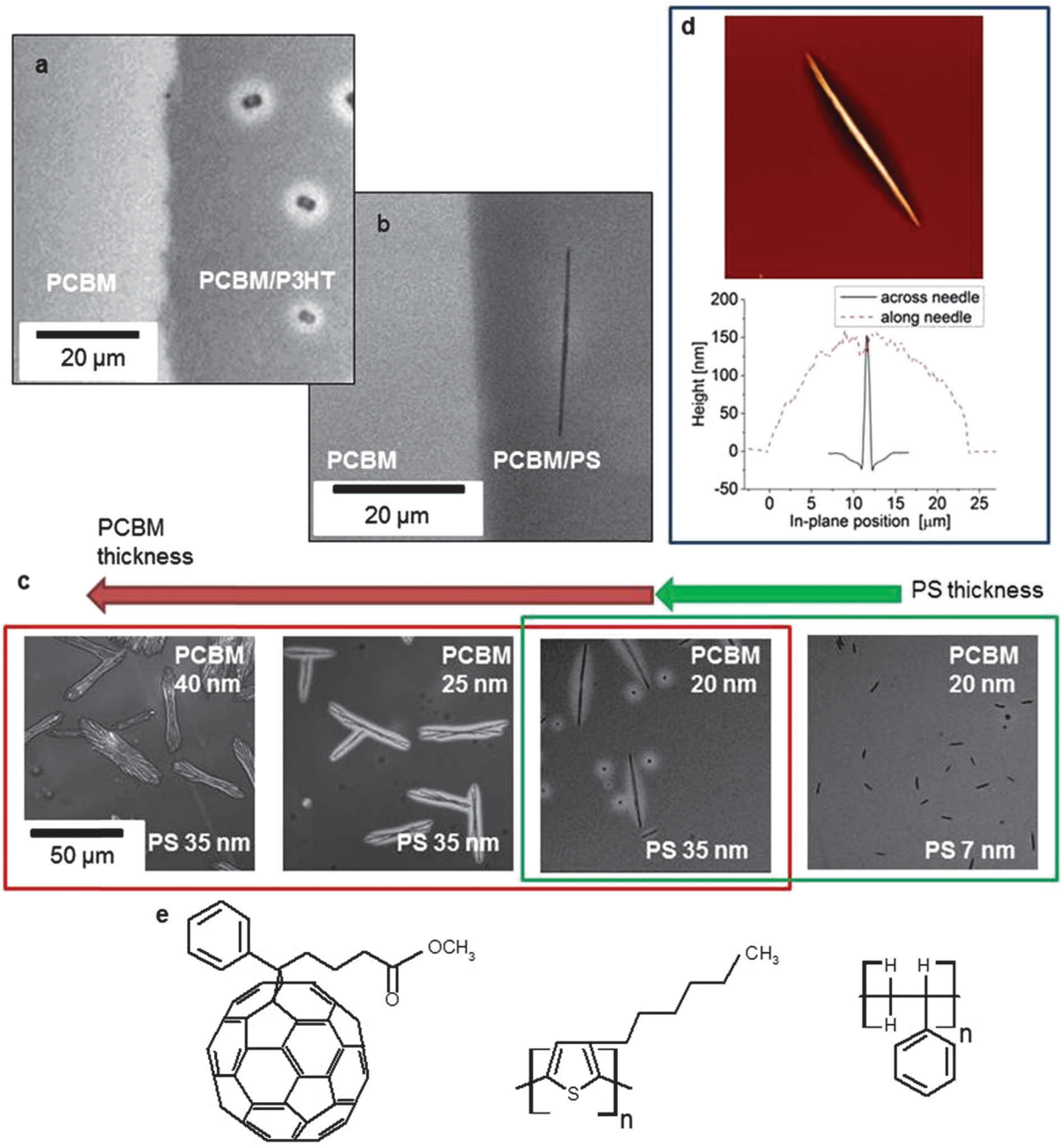

Fig. 1 Optical micrographs of silicon–PCBM–polymer bilayers. (a) A PCBM(20 nm)–P3HT(40 nm) bilayer annealed at 140 °C for 120 minutes. (b) A PCBM(20 nm)–PS(344k, 35 nm) bilayer annealed at 170 °C for 120 minutes. (c) PCBM–PS bilayers annealed at 170 °C for 120 minutes. (d) AFM topography image (30 μm × 30 μm scan) and height profiles across and along the main axis of a single PCBM needle in a PCBM(20 nm)–PS(344k, 26 nm) bilayer annealed at 170 °C for 24 minutes. These samples were all *ex situ* annealed (in the dark) and then imaged. (e) The chemical structures of PCBM, P3HT and PS (with degree of polymerization *n*).

The needle-like crystals show a characteristic shape of growth-curve, in which the growth-rate gradually declines from its maximum value following nucleation. Only isolated crystals were probed, so the gradual decline in growth-rate is not related to interference between the crystals. Given the potential sensitivity of fullerenes to UV and visible light,[36–38] we kept the illumination intensity from the microscope lamp as low as possible, and also performed control experiments in which duplicate samples were illuminated continuously and intermittently during annealing. Fig. 2d shows that the illumination did not significantly affect the growth-curves. In the PS bilayers, most crystals nucleate within the first twenty minutes of annealing, but some nucleate significantly later (see Fig. 2d). Examination of crystals that nucleate at significantly different times in polymer films thicker than 35 nm reveals that, on a given sample of this type, later-nucleated-crystals do not generally grow as long as earlier-nucleated-crystals. In Fig. 2d the growth-curve of the crystal nucleated at around 40 minutes matches the growth-curves of

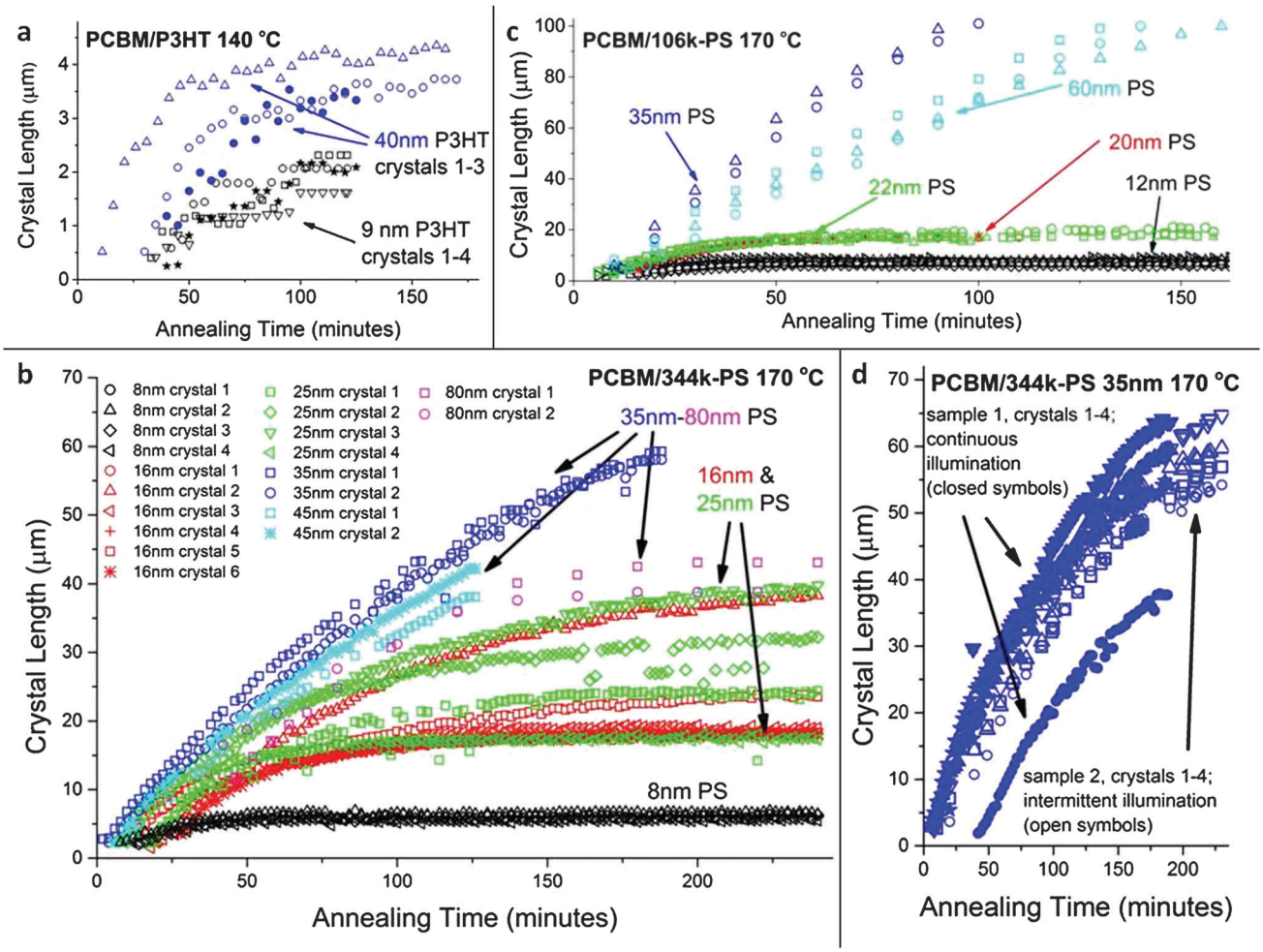

Fig. 2 *In situ* isothermal growth of isolated PCBM crystals. All figures plot the length along the dominant needle axis as a function of the time since annealing began. (a), (b) and (c) show a selection of crystals that nucleate at approximately the same time, for various polymer thicknesses. The 40 nm P3HT plots in (a) and the plots in (d) also show examples of crystals that nucleate after significantly different annealing-times. All plots have a 20 nm PCBM bottom layer with (a), a P3HT top layer, (b), (d) a 344k-PS top layer and (c) a 106k-PS top layer. (d) also compares growth-curves from duplicate samples imaged using two different illumination protocols (see Experimental methods for details). The labels crystal 1–crystal 6 represent different crystals on the same sample. These PS samples were all fabricated from the same batches of materials (batch 1), on silicon substrates that were prepared using a sonication/rinsing protocol (see Experimental methods for details).

the earlier-nucleated crystals when overlapped following displacement of the curve along the ordinate (see ESI,† Fig. S10). This signifies that the growth-rate of these crystals at a given time is a function of the sample annealing-time, and not of the time since crystal nucleation. This therefore suggests that the growth of the needle tips is not being slowed due to any changing property of the growing needle itself or its immediate surroundings (as occurs in diffusion-limited growth, due to depletion of material ahead of a growing crystal front[15]). It is instead impeded by changes in the properties of the bilayer into which the needle-like crystal is growing.

Bilayer composition profiles

One hypothesis to explain the PS-thickness-dependent growth-curves is that PCBM–PS mixing occurs, with the film composition having a dependence on annealing-time and on the initial polymer-film-thickness (leading to enhanced PCBM-molecular-mobility with higher PS concentration). To investigate the composition-profile normal to the substrate we performed a systematic series of NR measurements, using both *ex situ* and *in situ* annealed samples. The needle-like crystals occupy less than 1% of the area of the sample at the end of annealing in these experiments, enabling us to use NR to probe the structure of the remaining film into which the needles grow. Excellent fits to the NR data are obtained using a bilayer model in which the scattering-length-density (SLD) and thickness of both layers, plus the interfacial and surface roughness is allowed to vary. In the case of both the PCBM–P3HT bilayers and the PCBM–PS bilayers, NR reveals that there is transfer of PCBM into the polymer layer (ESI,† Fig. S11 and S12), in accord with previous observations for P3HT.[27,28,30–32] This transfer happens so rapidly that an isothermal transfer process cannot be properly characterized given the timescale of the temperature-ramp in the experiments (see ESI†). Comparison with optical microscopy shows that

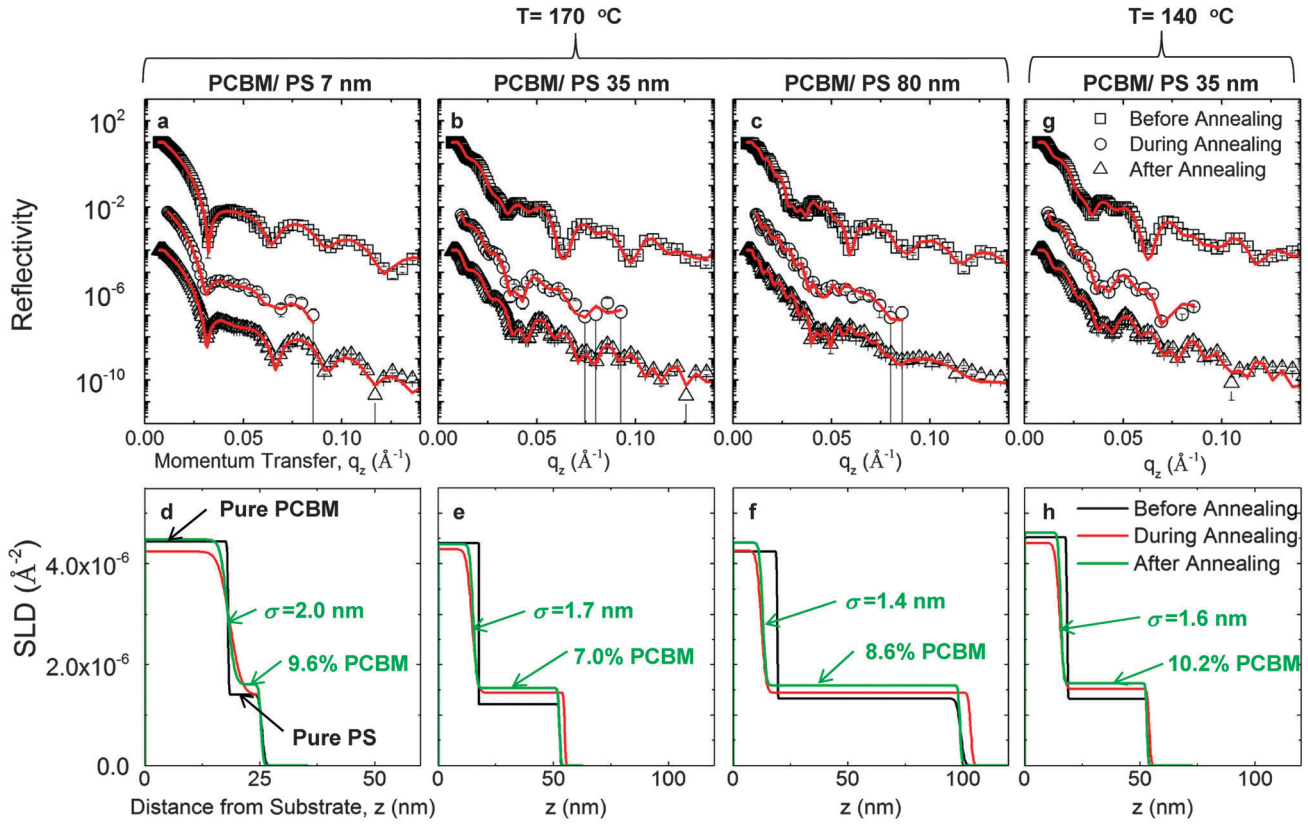

Fig. 3 NR measurements and fits for *in situ* annealed PCBM(20 nm)–PS(344k) on silicon. (a)–(c) Reflectivity *versus* momentum transfer normal to the substrate (q_z), for bilayers annealed at 170 °C. The SLD profiles corresponding to the best-fit lines in (a)–(c) are given in (d)–(f) respectively. (g), (h) Reflectivity and corresponding SLD profiles at 140 °C. The total (Gaussian) interface roughness, σ, of the PCBM/PS-rich-layer interface, and the percentage (by volume) of PCBM in the PS-rich layer after annealing (see ESI† for calculation details), is given in (d)–(f) and (h). Full reflectivity curves (using two incident angles) were measured before and after annealing, with measurements over a smaller q_z range (using a single incident angle) during annealing (see Experimental methods and ESI† for details). Reflectivity curves are offset with-respect-to the *y*-axis for clarity (top/middle/bottom curves corresponding to before/during/after annealing respectively). The reflectivity curves during annealing that are shown represent a total acquisition time of 15 minutes (combining 30 × 30 s time slices, during which the reflectivity curve did not change – see ESI†). SLD profiles for all samples have the substrate/PCBM interface at $z = 0$, an initial PCBM layer (before annealing) with SLD $\sim 4.4 \times 10^{-6}$ Å^{-2} between $z = 0$ and 20 nm, and initial PS layers of SLD $\sim 1.3 \times 10^{-6}$ Å^{-2} of varying thickness for $z \geq 20$ nm (black profile). The reflectivity scales for (b), (c) and (g) are the same as (a), and the SLD scales for (e), (f) and (h) are the same as (d).

this transfer occurs well before the observation of any micron-sized PCBM crystals. No further changes to the composition occurred as the samples were held at a constant temperature. The mixing behavior in the PCBM–P3HT system shows significant complexity as a function of temperature and film-thickness compared to the PCBM–PS system, probably due to the tendency of both components to crystallize.[8,14] We therefore focus here on the greater clarity given by the PCBM–PS results. All annealed PCBM–PS samples show an increase in the SLD of the top layer and a broadening of the interface between this layer and the PCBM bottom layer, in comparison to the unannealed bilayers. The PCBM–PS bilayers annealed at ~170 °C show the establishment of a similar composition (9.5 ± 1.4% PCBM) of the top (PS-rich) layer, and a similar interfacial-roughness of 1.6 ± 0.2 nm between this layer and a pure PCBM layer for all initial PS thicknesses (Fig. 3a–f and ESI,† Table S1 for further details). The establishment of a consistent profile between two compositions, independent of the starting PS-film-thickness is suggestive that this composition-profile represents a liquid–liquid equilibrium profile between a PS-rich phase and amorphous PCBM. This is further supported by the observation of a very similar composition-profile at ~140 °C (Fig. 3g and h). One can imagine that a similar equilibrium composition-profile (dependent on the Flory–Huggins interaction parameter and the polymer chain stiffness[39]) might exist at 140 °C and 170 °C. In contrast, an interface profile resulting from crystallization kinetics, (which ESI,† Fig. S1–S3 and Verploegen *et al.*[14] show are strongly temperature-dependent) would be less likely to produce a consistent profile over this temperature range.

PCBM nanocrystal growth

The NR results demonstrate that the different growth-rates of micron-sized PCBM needles are not a consequence of differences in PS-thickness leading to large differences in the local composition seen by the PCBM molecules.[40] An alternative explanation for the PS-thickness-dependent growth-rate is that the structure, rather than the composition, within the bilayer is strongly dependent on PS-film-thickness. PCBM nanocrystals

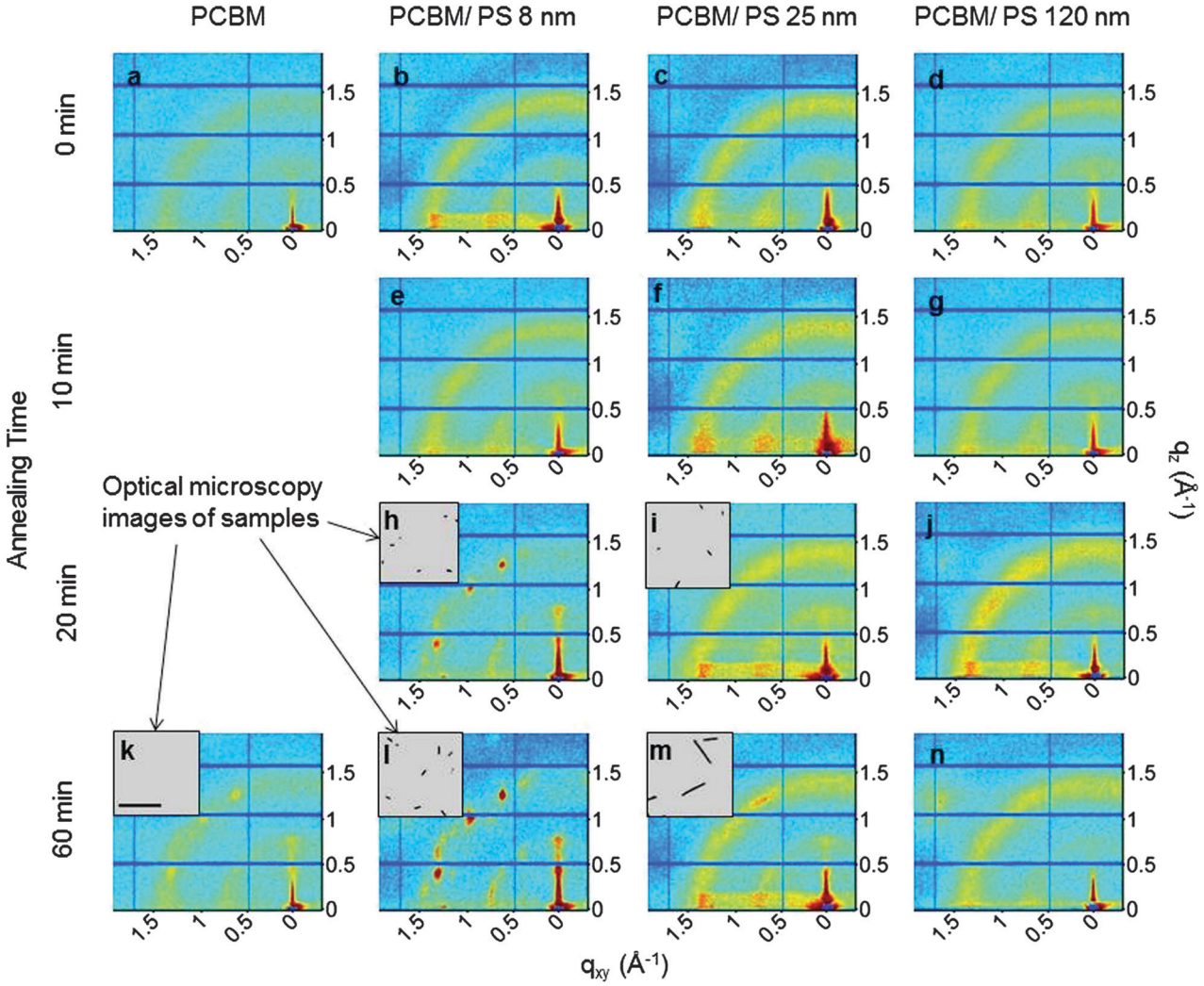

Fig. 4 Optical microscopy images and GIXD intensity maps (at an incident angle 0.19° – above the critical angle) from PCBM(20 nm)–PS(344k) bilayer samples and PCBM(20 nm) single layers on silicon, *ex situ* annealed at 170 °C. Crystallite sizes (given by Scherrer analysis – see ESI†) for the diffraction peaks after 60 minutes annealing in the PCBM single-layer, and bilayers with PS thickness 8 nm, 25 nm and 120 nm are 10 ± 5 nm, 11 ± 6 nm, 5 ± 3 nm and 3 ± 2 nm respectively. (a)–(n) are direct maps of the detector intensity, as displayed in the literature on PCBM blends.[8,14] The axis labels q_z and q_{xy} represent the out-of-plane and in-plane components of the momentum transfer respectively[8,14,41] (defined in the ESI†). The scale bar in the optical microscopy inset in (k) is 20 μm. The optical microscopy insets in (h), (i), (l) and (m) have the same scale as (k). An acquisition time of 10 s was used for all GIXD maps.

can form in PCBM–polymer blends.[7–9] We investigated nanocrystal growth within bilayers using GIXD, TEM and SAED. Fig. 4 shows GIXD measurements. Samples were measured *ex situ* after annealing. The unannealed bilayers show rings of intensity at $|\underline{q}| \sim 0.7$ Å^{-1} and $|\underline{q}| \sim 1.4$ Å^{-1} corresponding to first and second order diffraction from amorphous PCBM.[8,14,20,41,42] On annealing there is a dramatic difference in the diffraction as a function of the PS film-thickness. Diffraction spots are seen after 20 minutes annealing for 8 nm PS, with a further increase in the intensity of these spots after 60 minutes. The GIXD patterns show preferential crystalline orientation with-respect-to the substrate, as observed in PCBM–polymer blends[8,14] and share the strongest intensity peaks with the pure-PCBM film. For 8 nm PS there is a significant reduction in the amorphous PCBM intensity after 20 minutes and a further reduction after 60 minutes. Optical microscopy on these two samples shows needles only cover a small fraction of the sample surface. The 25 nm PS bilayers retain the amorphous PCBM ring, with no evidence of PCBM crystalline spots, after 20 minutes annealing. Optical microscopy shows the presence of needle-like crystals on this sample. By contrast, the annealed pure-PCBM sample shows PCBM diffraction spots, but no observable needle-like crystals. The lack of any correlation between the appearance of diffraction spots and the presence of micron-sized needles demonstrates that the spots are not due to the micron-sized needle-like crystals, but are instead due to crystals within the bilayer that are not resolved by optical microscopy. This is further evidenced by Scherrer analysis[6,8,43] (see ESI†), which reveals that the crystallite sizes responsible for the diffraction peaks in Fig. 4 are of order 10 nm. The GIXD results also support the

interpretation that the rapidly established composition-profile observed by NR is a liquid–liquid equilibrium profile. This is because the composition-profile is established before any crystal formation occurs (either micron-sized crystals in optical microscopy or nanocrystals *via* GIXD), and because the subsequent growth of crystals has no effect on the composition-profile observed by NR, for any thickness of PS.

Nanocrystal formation in-parallel with the preservation of an unchanging composition-profile would not occur if the PS-rich layer was the principal location for nanocrystal formation. In such a scenario the depletion of amorphous PCBM within this layer would lead to the re-establishment of an equilibrium composition-profile between the PCBM bottom-layer and the remaining amorphous part of the PS-rich top-layer, by the transfer of PCBM molecules into the top-layer. This would lead to a continually increasing PCBM concentration in the top-layer, which we do not observe. However, the influence of the polymer on the nanocrystal growth-rate is clear, and therefore the most plausible explanation for the unchanging composition-profile is that nanocrystal formation is mediated by the polymer at the PS/PCBM interface, but that the nanocrystals, once formed, stay within the 'bulk' of the PCBM layer, leaving an interface profile dominated by the equilibrium between amorphous PCBM and the PS-rich layer.

PCBM crystal growth on mica substrates: TEM and SAED

To further investigate the nature of crystal formation we performed TEM–SAED measurements on bilayers annealed on mica substrates. Although the potential influence of the substrate[16] means that these samples are not exact duplicates of the bilayers on silicon, annealing reveals similar needle-like crystals with lengths of order tens-of-microns (ESI,† Fig. S17). TEM on PCBM–PS bilayers resolves two distinct crystal forms on smaller lengthscales. Fig. 5a shows part of a micron-sized needle, with a similar (single-crystal) SAED pattern to that observed previously in PCBM–polymer blends.[35] Fig. 5b–d show typical TEM images from regions away from the micron-sized needles. The fields of view are populated by both low-aspect-ratio crystals and

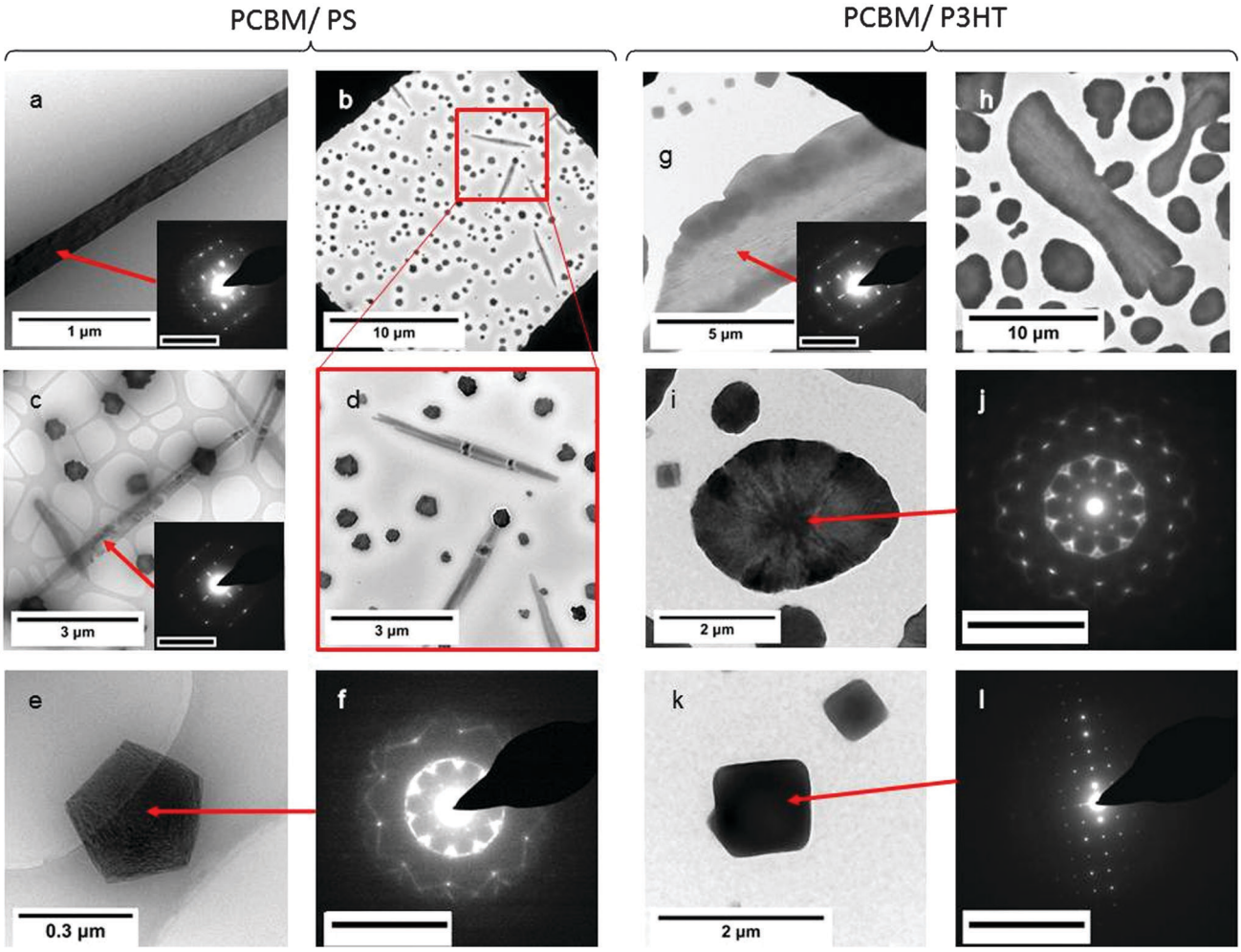

Fig. 5 TEM–SAED of PCBM(20 nm)–polymer bilayers annealed on mica substrates. (a) A 35 nm 344k-PS bilayer annealed at 190 °C for 120 minutes. (b)–(f) A 35 nm 344k-PS bilayer annealed at 170 °C for 24 hours. (g)–(l) A 40 nm P3HT bilayer annealed at 140 °C for 24 hours. The scale bars shown with the SAED patterns in (a), (c), (f), (g), (j) and (l) have a length of 0.3 $Å^{-1}$. The samples in (c), (e) and (f) were prepared on a TEM grid with a holey-carbon support film.

needle-like crystals. Closer inspection of the low-aspect-ratio crystals reveals a pentagonal shape (Fig. 5e). Fig. 5f shows the SAED from one of these crystals, showing that it has a different diffraction pattern (but with similar *d*-spacings; see ESI†) to the needle-like crystals, with 5-fold (plus inversion) symmetry.

TEM–SAED measurements on PCBM–P3HT bilayers also reveal the existence of different types of crystal. In PCBM–P3HT bilayers we see the co-existence of cubic crystals on nano-to-micron length-scales, with higher aspect-ratio needles (albeit less well-defined than for PS) on micron to tens-of-micron length-scales, and more isotropic-looking structures showing 5-fold symmetry at intermediate scales (with the same diffraction peaks as PCBM–PS; see Fig. 5g and j). The existence of different kinds of PCBM crystal in PCBM–polymer blends annealed on mica, including pentagonal and cubic structures for PS and P3HT, was observed recently, with crystal-twin formation proposed to explain the observed 5-fold symmetry.[16] Zheng *et al.*[16] uncover a rich diversity in PCBM crystal structure and morphology within blends, as a function of annealing-temperature, substrate-type and average-composition. The further study of bilayers, containing a simpler and better-characterized film-composition-profile, could contribute significantly towards a fuller understanding of polymer-mediated PCBM crystallization. In terms of the present study, it is clear that there is strong evidence from optical microscopy, GIXD and TEM–SAED that crystals of a different form can co-exist within bilayers between the larger needle-like crystals. The restricted growth of low-aspect-ratio crystals in comparison with the needles may be due to an orientation of these crystals such that the fast-growth-direction is normal to the substrate, which would slow growth in the substrate-plane of itself, and also due to the development of a depletion-region ahead of a growing low-aspect-ratio crystal. Crystal-twinning (where, for example, decahedra form from 5 twinned tetradehra, as seen in a variety of systems[44] including fullerenes[45]) may also restrict crystal growth, compared to single-crystals, *via* internal strain at the twin boundaries.[44]

Modeling bimodal crystal-growth kinetics

In the silicon–PCBM–PS system, it is clear that the growth of both nano- and micron-sized PCBM crystals is strongly influenced by the thickness of the PS layer. We believe that the interaction between crystals is crucial to understanding the needle growth process. TEM images from the mica-annealed samples show evidence that crystals (both needles and low-aspect-ratio crystals) can exist in different planes within the film, sometimes growing past one another unhindered (Fig. 5c), and sometimes clearly interfering with one another (Fig. 5d). We propose that in the silicon–PCBM–PS system it is the increased volume-fraction of nanocrystals in the surrounding PCBM layer that hinders needle growth. The process is not abrupt and we therefore propose that the increasing solids-content in the PCBM layer leads to an increased film-viscosity, progressively slowing the growth of the micron-sized needle-like crystals.[46]

Fig. 6a shows a selection of the *in situ* needle-like crystal growth-curves fitted using a simple model for the film-viscosity as a function of time. This model (further details are given in the ESI†) combines Avrami kinetics[14,47–49] for the growth of the nanocrystalline volume-fraction, ϕ, and suspension rheology for the dependence of viscosity on ϕ.[50] The growth-rate of the needles in this model is inversely-proportional to the effective-viscosity of the film into which the needles are growing, and is given by

$$\frac{\mathrm{d}l}{\mathrm{d}t} = A\left(\phi_m - 1 + \mathrm{e}^{-(Kt)^n}\right)^m, \qquad (1)$$

where n and K are the Avrami exponent and growth-rate respectively, ϕ_m is the nanocrystal volume-fraction at which the effective viscosity diverges, A is a prefactor that is inversely proportional to the effective-viscosity of the film in the absence of nanocrystals, and m is the exponent in the suspension-viscosity model.[51] The integral of eqn (1) was simultaneously fitted to 61 individual crystal datasets, in which the parameters n, m and ϕ_m were the same for all datasets, while A, K and the integration constant l_0 (determined by the needle nucleation-time) were allowed to vary independently. In accordance with the idealized theory[52] we fixed the exponent n at integer values between one and four. Best-fits were obtained with $n = 1$, giving good agreement with the 61 growth-curves, representing different thicknesses and two different M_ws of PS (Fig. 6a). The prefactor A (Fig. 6b) shows no strong dependence on PS film-thickness or M_w, implying that the mechanics of the needle-growth/film-deformation process are largely controlled by the properties of the PCBM layer.[53] However, the nanocrystal growth-rate K shows a significant increase with decreasing PS thickness that is similar for both M_ws (Fig. 6c). An order-of-magnitude estimate of K can also be obtained by directly estimating ϕ from the GIXD measurements and fitting ϕ-*versus*-time data with the ($n = 1$) Avrami equation (see ESI† for details). Although the data is limited, this shows broad agreement with the optical microscopy K parameter, in terms of magnitude and corroboration of the PS-thickness-dependence (see Fig. 6c).

Given the evidence from multiple techniques and modeling, it seems clear that our findings are well-described by a picture in which the continued growth of the nanocrystal volume-fraction within the PCBM layer steadily reduces the growth-rate of the micron-sized needle-like crystals. This leaves the question; why, given the consistent composition-profile across the PCBM/PS interface, does the thickness of the PS-rich top-layer have such an impact on the growth of the nanocrystals within the PCBM bottom-layer? We are unable to give a definitive answer to this question at present, but our thoughts on potential explanations are as follows; It is in-principle possible that a high level of sensitivity to PS-thickness-dependent subtleties within the bilayer structure, could be responsible for the dependence of crystal-growth on PS-thickness. For instance, PS-thickness-dependent differences in the *nature* of the interface-composition-profiles (*e.g.*; different contributions from lateral-interface-roughness and molecular-level-mixing that somehow combine to give the similar *total*-interface-roughnesses that are measured by NR[39]) could occur, and impact (nano) crystallization-kinetics. However, we believe that a potentially more plausible explanation for the *K versus* PS-thickness behavior may arise from film-thickness-dependent molecular-mobility. Increased mobility at temperatures below the bulk T_g has been reported extensively for

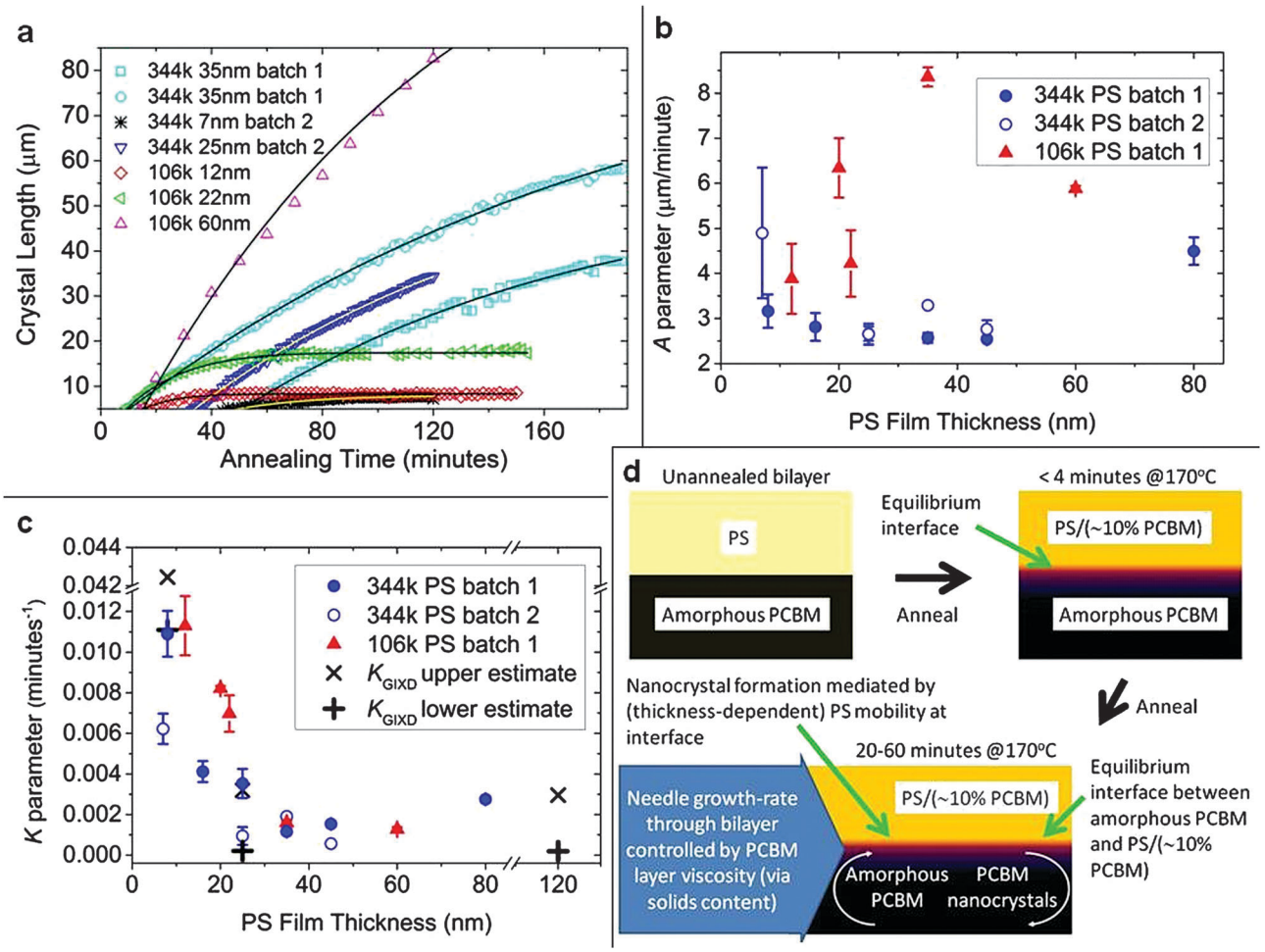

Fig. 6 Simultaneous fit results for silicon–PCBM–PS bilayers annealed at 170 °C. (a) Optical microscopy growth-curves and fits for a selection of the 61 simultaneously-fitted PCBM needles that have nucleated at various times and then grown in different M_w and thickness PS bilayers. These fits had the following eqn (1) fit parameters shared by all 61 datasets; $n = 1$ (fixed), $m = 3.4$, $\phi_m = 0.63$. (b), (c) Mean fit parameters A and K respectively, as a function of PS thickness and M_w. (c) also shows upper and lower estimates of the Avrami growth-rate parameter extracted from the GIXD data in Fig. 4, K_{GIXD}, as a function of PS thickness for 344k-PS (details of the calculation of the upper and lower estimates of K_{GIXD} are given in the ESI†). (d) Schematic diagram representing the evolution of the bilayer during annealing and the impact on needle-like crystal growth, with a tentatively-suggested mechanism for enhanced nanocrystal-growth within the PCBM layer, due to increased polymer-chain-mobility at the PCBM/PS-rich interface in the thinner PS films. Batch 1 refers to the same batch of samples that are shown in Fig. 2. Batch 2 refers to samples made with a different batch of PCBM, and with the silicon substrates used as-received.

polymer thin-films, over the last two decades.[23,24,54,55] We suggest this possible mechanism owing to the close correspondence between the thickness-dependence in Fig. 6c and the reported reductions in T_g (due to enhanced mobility at free-interfaces[24]) for PS thin-films.[23] This correspondence includes both the PS-thickness-dependence (significant deviations from 'bulk' T_g are observed for supported PS films with thickness below around 20–30 nm[23,55]) and the lack of strong M_w-dependence (for $M_w < 378\,000$ the T_g *versus* film-thickness behavior shows no M_w-dependence for both supported and free-standing PS films[55]). Computational and experimental studies of interfacial-mobility at higher temperatures in polymer melts are yet to reach consensus.[54] However, our findings are consistent with the possibility that increased polymer-chain-mobility within nanocomposite thin-films at temperatures well-above the pure-polymer T_g, may be the cause of the enhanced nanocrystal-growth-rate. If so, the absence of a strong M_w-dependence for the two (entangled) polymers suggests that polymer-chain-mobility on a length-scale below the polymer 'tube-diameter' (~8.5 nm for PS[33]) is key. This leads to a tentatively-suggested mechanism (see Fig. 6d) in which nanocrystal-growth within the PCBM layer is enhanced, due to increased polymer-chain-mobility at the PCBM/PS-rich interface in thin PS-nanocomposite films.

Conclusion

In summary, by performing a systematic investigation of the composition-profile in a bilayer geometry we have found strong evidence for the existence of a liquid–liquid polymer/fullerene equilibrium interface. Subsequent competitive-fullerene-crystallization on two different length-scales exhibits a strong

polymer-film-thickness dependence. These findings demonstrate the importance of considering free-interface/confinement effects when seeking to optimize nano- and micron-scale structure within polymer–fullerene optoelectronic devices. More broadly, the findings are an important contribution to understanding the science of polymer-nanocomposites near interfaces and in thin-films, and have potential significance in a wide range of applications, such as self-healing films[3] and nanocomposite electrolytes.[1] It may also prove possible to exploit this knowledge by *controlling* (*e.g.* patterning) confinement/interface-effects locally, to tune kinetics and hence structure in polymer-nanocomposite materials applications.

Acknowledgements

We acknowledge Leeds EPSRC Nanoscience and Nanotechnology Facility (LENNF) for providing access to TEM instrumentation and support. We thank the staff at the beam-lines IO7 at Diamond Light Source and D17 at ILL for their support during the experiments. DM and AMH thank Huw Summers for use of his optical microscope and Chris Wright for use of his AFMs. DM and AMH thank João Cabral, Him Cheng Wong, Rajeev Dattani, Alysin Nedoma and Jack Douglas for helpful discussions. AH thanks João Cabral for a critical reading of the manuscript. DM acknowledges EPSRC for funding his studentship *via* the Doctoral Training Grant to Swansea University.

References

1 F. Croce, G. B. Appetecchi, L. Persi and B. Scrosati, *Nature*, 1998, **394**, 456–458.
2 T. C. Merkel, *Science*, 2002, **296**(5567), 519–522.
3 S. Gupta, Q. Zhang, T. Emrick, A. C. Balazs and T. P. Russell, *Nat. Mater.*, 2006, **5**(3), 229–233.
4 N. D. Treat, J. A. Nekuda Malik, O. Reid, L. Yu, C. G. Shuttle, G. Rumbles, C. J. Hawker, M. L. Chabinyc, P. Smith and N. Stingelin, *Nat. Mater.*, 2013, **12**(7), 628–633.
5 K. Vandewal, S. Himmelberger and A. Salleo, *Macromolecules*, 2013, **46**(16), 6379–6387.
6 W. Yin and M. Dadmun, *ACS Nano*, 2011, **5**(6), 4756–4768.
7 X. N. Yang, J. K. J. van Duren, M. T. Rispens, J. C. Hummelen, R. A. J. Janssen, M. A. J. Michels and J. Loos, *Adv. Mater.*, 2004, **16**(9–10), 802–806.
8 P. E. Hopkinson, P. A. Staniec, A. J. Pearson, A. D. F. Dunbar, T. Wang, A. J. Ryan, R. A. L. Jones, D. G. Lidzey and A. M. Donald, *Macromolecules*, 2011, **44**(8), 2908–2917.
9 Y. Kim, J. Nelson, T. Zhang, S. Cook, J. R. Durrant, H. Kim, J. Park, M. Shin, S. Nam, M. Heeney, I. McCulloch, C.-S. Ha and D. D. C. Bradley, *ACS Nano*, 2009, **3**, 2557–2562.
10 E. Klimov, W. Li, X. Yang, G. G. Hoffmann and J. Loos, *Macromolecules*, 2006, **39**(13), 4493–4496.
11 J. J. Richards, A. H. Rice, R. D. Nelson, F. S. Kim, S. A. Jenekhe, C. K. Luscombe and D. C. Pozzo, *Adv. Funct. Mater.*, 2013, **23**(4), 514–522.
12 A. Swinnen, I. Haeldermans, M. vande Ven, J. D'Haen, G. Vanhoyland, S. Aresu, M. D'Olieslaeger and J. Manca, *Adv. Funct. Mater.*, 2006, **16**(6), 760–765.
13 C. H. Woo, B. C. Thompson, B. J. Kim, M. F. Toney and J. M. J. Frechet, *J. Am. Chem. Soc.*, 2008, **130**(48), 16324–16329.
14 E. Verploegen, R. Mondal, C. J. Bettinger, S. Sok, M. F. Toney and Z. Bao, *Adv. Funct. Mater.*, 2010, **20**(20), 3519–3529.
15 B. Watts, W. J. Belcher, L. Thomsen, H. Ade and P. C. Dastoor, *Macromolecules*, 2009, **42**(21), 8392–8397.
16 L. Zheng, J. Liu and Y. Han, *Phys. Chem. Chem. Phys.*, 2013, **15**(4), 1208–1215.
17 J. Zhao, A. Swinnen, G. Van Assche, J. Manca, D. Vanderzande and B. Van Mele, *J. Phys. Chem. B*, 2009, **113**(6), 1587–1591.
18 F. C. Jamieson, E. B. Domingo, T. McCarthy-Ward, M. Heeney, N. Stingelin and J. R. Durrant, *Chem. Sci.*, 2012, **3**(2), 485–492.
19 J. W. Kiel, A. P. R. Eberle and M. E. Mackay, *Phys. Rev. Lett.*, 2010, **105**(16), 168701.
20 J. A. Bartelt, Z. M. Beiley, E. T. Hoke, W. R. Mateker, J. D. Douglas, B. A. Collins, J. R. Tumbleston, K. R. Graham, A. Amassian, H. Ade, J. M. J. Fréchet, M. F. Toney and M. D. McGehee, *Adv. Energy Mater.*, 2013, **3**(3), 364–374.
21 S. Himmelberger, J. Dacuña, J. Rivnay, L. H. Jimison, T. McCarthy-Ward, M. Heeney, I. McCulloch, M. F. Toney and A. Salleo, *Adv. Funct. Mater.*, 2013, **23**(16), 2091–2098.
22 A. Ashraf, D. M. N. M. Dissanayake, D. S. Germack, C. Weiland and M. D. Eisaman, *ACS Nano*, 2014, **8**(1), 323–331.
23 J. L. Keddie, R. A. L. Jones and R. A. Cory, *Europhys. Lett.*, 1994, **27**(1), 59–64.
24 O. Baumchen, J. D. McGraw, J. A. Forrest and K. Dalnoki-Veress, *Phys. Rev. Lett.*, 2012, **109**(5), 055701.
25 M. Campoy-Quiles, M. Sims, P. G. Etchegoin and D. D. C. Bradley, *Macromolecules*, 2006, **39**(22), 7673–7680.
26 T. Wang, A. J. Pearson, A. D. F. Dunbar, P. A. Staniec, D. C. Watters, D. Coles, H. Yi, A. Iraqi, D. G. Lidzey and R. A. L. Jones, *Eur. Phys. J. E*, 2012, **35**(12), 129.
27 D. Chen, A. Nakahara, D. Wei, D. Nordlund and T. P. Russell, *Nano Lett.*, 2011, **11**(2), 561–567.
28 H. Chen, R. Hegde, J. Browning and M. D. Dadmun, *Phys. Chem. Chem. Phys.*, 2012, **14**(16), 5635–5641.
29 B. A. Collins, E. Gann, L. Guignard, X. He, C. R. McNeill and H. Ade, *J. Phys. Chem. Lett.*, 2010, **1**(21), 3160–3166.
30 K. H. Lee, P. E. Schwenn, A. R. G. Smith, H. Cavaye, P. E. Shaw, M. James, K. B. Krueger, I. R. Gentle, P. Meredith and P. L. Burn, *Adv. Mater.*, 2011, **23**(6), 766–770.
31 H. W. Ro, B. Akgun, B. T. O'Connor, M. Hammond, R. J. Kline, C. R. Snyder, S. K. Satija, A. L. Ayzner, M. F. Toney, C. L. Soles and D. M. DeLongchamp, *Macromolecules*, 2012, **45**(16), 6587–6599.
32 N. D. Treat, M. A. Brady, G. Smith, M. F. Toney, E. J. Kramer, C. J. Hawker and M. L. Chabinyc, *Adv. Energy Mater.*, 2011, **1**(1), 82–89.
33 M. Rubinstein and R. H. Colby, *Polymer Physics*, Oxford University Press, Oxford, 1st edn, 2003.
34 H. Zhong, X. Yang, B. deWith and J. Loos, *Macromolecules*, 2006, **39**, 218–223.

35 L. Li, G. Lu, S. Li, H. Tang and X. Yang, *J. Phys. Chem. B*, 2008, **112**(49), 15651–15658.
36 Z. Li, H. C. Wong, Z. Huang, H. Zhong, C. H. Tan, W. C. Tsoi, J. S. Kim, J. R. Durrant and J. T. Cabral, *Nat. Commun.*, 2013, **4**, 2227.
37 H. C. Wong, A. M. Higgins, A. R. Wildes, J. F. Douglas and J. T. Cabral, *Adv. Mater.*, 2013, **25**(7), 985–991.
38 H. C. Wong, Z. Li, C. H. Tan, H. Zhong, Z. Huang, H. Bronstein, I. McCulloch, J. T. Cabral and J. R. Durrant, *ACS Nano*, 2014, **8**, 1297–1308.
39 R. A. L. Jones and R. W. Richards, *Polymers at Surfaces and Interfaces*, Cambridge University Press, Cambridge, 1st edn, 1999.
40 We also checked that the reduction in the thickness of the PCBM layer due to migration of PCBM into the PS-rich layer is not responsible for the observed growth-rate differences (ESI,† Fig. S13).
41 S. Lilliu, T. Agostinelli, E. Pires, M. Hampton, J. Nelson and J. E. Macdonald, *Macromolecules*, 2011, **44**(8), 2725–2734.
42 M. T. Rispens, A. Meetsma, R. Rittberger, C. J. Brabec, N. S. Sariciftci and J. C. Hummelen, *Chem. Commun.*, 2003, 2116–2118.
43 H. P. Klug and L. E. Alexander, *X-ray Diffraction Procedures for Polycrystalline and Amorphous Materials*, Wiley, New York, 2nd edn, 1974.
44 C. Lofton and W. Sigmund, *Adv. Funct. Mater.*, 2005, **15**, 1197–1208.
45 B. Pauwels, D. Bernaerts, S. Amelinckx, G. V. Tendeloo, J. Joutsensaari and E. I. Kauppinen, *J. Cryst. Growth*, 1999, **200**, 126–136.
46 An alternative suggestion, proposed by Richards *et al.* (ref. 11) for slowing of PCBM needle growth in blends, is that the reduced volume fraction of amorphous PCBM itself directly affects the growth-rate, without the need to consider the viscosity increase. This explanation would imply that flow of material is unimportant within the nanocrystalline/amorphous PCBM layer, but rather that the micron-sized needle simply grows through the steadily diminishing amorphous fraction of the PCBM, without displacement of the existing nanocrystals. However, significant flow of material clearly takes place, as evidenced by the shape of the PCBM needles. Also, there is no diminution of the single crystal nature of the needles with time. Optical microscopy under crossed-polars reveals no transition from birefringent to isotropic properties as the needle tip is approached (Fig. S8 and S9, ESI†), implying that nanocrystals are not incorporated within the growing needles. This is further supported by the unchanging shape of the growing needle tip as a function of time (Fig. S7, ESI†), which would not be expected if the needles were progressively incorporating more nanocrystals.
47 H. C. Wong and J. T. Cabral, *Macromolecules*, 2011, **44**(11), 4530–4537.
48 W.-R. Wu, U. S. Jeng, C.-J. Su, K.-H. Wei, M.-S. Su, M.-Y. Chiu, C.-Y. Chen, W.-B. Su, C.-H. Su and A.-C. Su, *ACS Nano*, 2011, **5**(8), 6233–6243.
49 M. Avrami, *J. Chem. Phys.*, 1941, **9**, 177–184.
50 I. M. Krieger and T. J. Dougherty, *Trans. Soc. Rheol.*, 1959, **3**, 137–152.
51 The exponent m is equal to the product of the intrinsic viscosity and ϕ_m, and depends on the shape of the suspended particles (see H. A. Barnes, J. F. Hutton and K. Walters, *An Introduction to Rheology*, Elsevier, 1st edn, 1989).
52 M. Avrami, *J. Chem. Phys.*, 1940, **8**, 212–224.
53 The fitted A parameters shown in Fig. 6b are in-general larger for crystals on the 106k-PS samples in comparison with the 344k-PS samples. The ratios A^{106k}/A^{344k} at a given PS thickness are in the range one-to-3.5. This compares with a ratio of the inverse of the bulk zero-shear-rate viscosities of these PS M_ws of 55.
54 M. D. Ediger and J. A. Forrest, *Macromolecules*, 2014, **47**, 471–478.
55 J. A. Forrest and K. Dalnoki-Veress, *Adv. Colloid Interface Sci.*, 2001, **94**(1–3), 167–196.